Chemical vapor deposition of silicon carbide on alumina ultrafiltration membranes for filtration of microemulsions

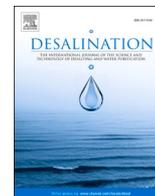Qin, Guangze; Jan, Asif; An, Qi; Zhou, H.; Rietveld, Luuk C.; Heijman, Sebastiaan G. J.

Important note
To cite this publication, please use the final published version (if applicable).
Please check the document version above.

Chemical vapor deposition of silicon carbide on alumina ultrafiltration membranes for filtration of microemulsions

Guangze Qin [a,*], Asif Jan [a], Qi An [b], Hanxiao Zhou [a], Luuk C. Rietveld [a], Sebastiaan G. J. Heijman [a]

[a] Section of Sanitary Engineering, Department of Water Management, Faculty of Civil Engineering and Geosciences, Delft University of Technology, Stevinweg 1, 2628 CN Delft, the Netherlands
[b] Section of Complex Fluid Processing, Department of Process & Energy, Faculty of Mechanical, Maritime and Materials, Delft University of Technology, 2628 CN Delft, the Netherlands

HIGHLIGHTS

- Ultrathin (18 nm) polycrystalline 3C-SiC was deposited onto a Al_2O_3 membrane.
- SiC membrane with the smallest pore size (33 nm) for oil/water separation.
- Highly hydrophilic membranes with a negative surface charge were produced.
- Various pore sizes of 3C-SiC coated membranes were compared.
- A combination of high oil rejection and low (ir)reversible fouling was achieved.

GRAPHICAL ABSTRACT
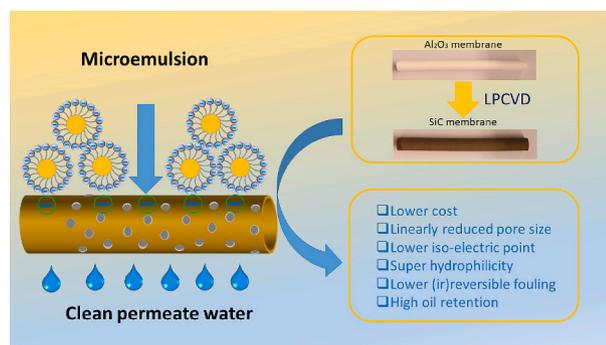
ARTICLE INFO

ABSTRACT

Worldwide, a considerable amount of oily wastewater is generated, with oil droplets from 2 to 200 nm that are difficult to separate because of their size and colloidal stability. This study presents a novel approach for effectively separating microemulsions via cubic silicon carbide (3C-SiC)-coated alumina (Al_2O_3) membranes fabricated based on low pressure chemical vapor deposition (LPCVD). SiC was deposited at a relatively low temperature at 860 °C on 100 nm Al_2O_3 membranes using two precursors: SiH_2Cl_2 and C_2H_2. With the increase in deposition time, up to 25 min, the pore size decreased from 41 nm to 33 nm, which is a smaller pore size of a SiC membrane than previously used for oil/water separation. The polycrystalline 3C-SiC-coated membranes showed improved hydrophilicity (water contact angle of 15°) and highly negatively charged surfaces (−65 mV). Microemulsion filtration experiments were carried out at a constant permeate flux (80 $Lm^{-2} h^{-1}$) for six cycles with varying deposition time, pH, surfactant types, and pore sizes. The fouling of the SiC-coated membrane was, compared to the Al_2O_3 membrane, effectively mitigated due to the enhanced electrostatic repulsion and hydrophilicity. Surfactant adsorption mainly occurred when the surface charge of the microemulsion and the membranes were opposite. Therefore, the surface charge of the alumina membrane changed from positive to negative when soaked in negatively charged microemulsions, whereas SiC-coated membranes remained

* Corresponding author.
 E-mail address: G.Qin@tudelft.nl (G. Qin).

negatively charged regardless of surfactant type. The membrane fouling was alleviated when the membrane and oil droplets had the same charge. Lastly, the 62 nm SiC-coated membrane with 20 min coating time was the best choice for the filtration of the microemulsion, because of the high rejection of the oil droplets and low fouling tendency.

Nomenclature

List of symbols

D	Diameter of membrane pores (m)
J	Permeate flux (Lm^{-2} h^{-1})
$L_{p,20\,°C}$	Water permeance at 20 °C (Lm^{-2} h^{-1} bar^{-1})
P	Applied pressure (N/m^2)
R	Resistance to mass transfer (m^{-1})
T	Water temperature (°C)

Greek letters

μ	Permeate viscosity (Pa·s)
γ	Surface tension of the wetting liquid (N/m)
θ	Contact angle (°)

Abbreviations

AFM	Atomic force microscopy
Al$_2$O$_3$	Alumina
CFV	Crossflow velocity
COD	Chemical oxygen demand
CTAB	Cetyltrimethylammonium bromide
DI	Demineralized
EDX	Energy Dispersive X-ray
IEP	The isoelectric point
LPCVD	Low pressure chemical vapor deposition
MF	Microfiltration
O/W	Oil-in-water
PSD	Particle size distribution
SiC	Silicon carbide
SDS	Sodium dodecyl sulfate
TEM	Transmission electron microscopy
TF	Threshold flux
TMP	Transmembrane pressure
UF	Ultrafiltration
UOCA	Underwater oil contact angle
WCA	Water contact angle
XRD	X-ray Diffraction

---

1. Introduction

Worldwide, oily wastewater is generated from the petrochemical, pharmaceutical, food, and beverage industries [1,2]. However, the discharge of oily wastewater can severely contaminate groundwater and surface water and is harmful to human health [3,4]. At present, the typical and conventional technologies for the treatment of oily wastewater include (i) dissolved air flotation [5], (ii) gravity-based separation [6], (iii) hydrocycloning [7], and (iv) adsorption [8]. The choice between the various oil-water separation technologies depends on oil droplet size/concentration, properties of oily wastewater, and the maximum allowable emission concentration [9,10]. Meanwhile, the emerging membrane separation technology is regarded as a promising and sustainable approach for effectively treating wastewater due to its distinct advantages, including a small footprint and high separation efficacies [11,12]. Compared with polymeric membranes, inorganic ceramic membranes have attracted increasing attention due to their high mechanical/chemical stability, hydrophilicity and water permeance [1,13,14].

Most oil-in-water (O/W) emulsions have oil droplet sizes ranging from a few nanometers to several hundred micrometers. For emulsions with micron-sized oil droplets, ceramic ultra/microfiltration (UF/MF) membranes show satisfactory rejection, typically in the range of 90–99 % [9,15]. However, some industrial operations also generate large quantities of oily wastewater with oil droplets from 2 to 200 nm [16]. These emulsions are predominantly thermodynamically stable "microemulsions" with sizes ranging from 10 to 100 nm [16,17]. So effective and widely applicable strategies for separating different emulsions with nano-sized oil droplets are highly required. Some studies [1,18–20] have addressed the treatment of nano-sized oil emulsions using inorganic membranes such as zirconia and carbon nanotubes. Silicon carbide (SiC) membranes are usually fabricated using the sol-gel technique at a high temperature (up to 2100 °C), resulting in long production times and high costs [21]. To save costs and diminish the environmental impact of membrane production, in our previous work, we developed an innovative method for producing a SiC coating based on low pressure chemical

vapor deposition (LPCVD) onto Al$_2$O$_3$ UF membranes at 750 °C. In addition, our previous studies found that the SiC-coated alumina (Al$_2$O$_3$) membranes perform better than the Al$_2$O$_3$ membranes in separating micro-sized SDS stabilized oil/water emulsions with lower reversible and irreversible fouling [9]. However, on the one hand, the SiC layer deposited at 750 °C, which was reported in our previous studies, was not chemically stable due to the amorphous structure of SiC [15]. It has also been reported that 3C cubic and 6H hexagonal are the most stable structures compared with other SiC polytypes [22]. To solve this problem, the deposition temperature was increased from 750 °C to 860 °C to deposit the polycrystalline 3C-SiC on the 100 nm Al$_2$O$_3$ membrane surface [23]. The fouling behavior of the filtration of microemulsions using SiC-coated UF membranes has not yet been performed and reported. Therefore, we developed 3C-SiC membranes with smaller pore sizes and similar permeabilities compared with the previous work, to achieve high rejection of nano-sized emulsions.

Fouling is the main constraint when using membranes for oil-water separation [24]. One possible way to address fouling is to modify the wetting property of the membrane surface by coating hydrophilic materials, rich in hydroxyl groups (e.g., ZrO$_2$ and TiO$_2$ nanoparticles) [1,25]. Pore size is another critical factor influencing fouling [26–28]. Jiang et al. reported that SiC membranes with the largest pore size (0.67 μm) showed the highest flux decline rate and lowest stable flux when filtering 500 pm O/W emulsion at a constant pressure of 0.5 bar [28]. Nagasawa et al. also reported that severe fouling was induced for porous TiO$_2$ membranes with the largest pores (1.4 μm) since more oil droplets accumulated into the pores, leading to a high irreversible fouling [26]. However, studies on the effect of pore size on O/W emulsion separation in a crossflow, constant flux mode are lacking. Therefore, the objective of this study was to better understand the effect of surface charge, hydrophilicity, and pore size of the SiC-coated UF membranes on membrane fouling by O/W microemulsions in a constant flux mode. Firstly, deposition times determine the layer thickness, affecting the pore size and permeabilities of the membranes. Therefore, deposition times ranging from 10 to 25 min were employed to tune membrane pore sizes and surface properties. The effect of deposition time on membrane fouling was investigated to find the optimum deposition time. We then

evaluated ceramic membranes in terms of pore size, surface morphology, water permeance, mechanical strength, surface charge, and water contact angle before the filtration experiments. These experiments were conducted in crossflow filtration with constant fluxes for the filtration of O/W microemulsions, stabilized with anionic, cationic, and non-ionic surfactants. The effect of pH of the feed solution on fouling was also studied to find which types of oily wastewater (alkaline or acidic) are much more suitable for the treatment by SiC-coated membranes. Finally, by comparing the oil rejection and (ir)reversible fouling, the best pore size was chosen.

2. Materials and methods

2.1. Materials

Soybean oil (S7381, Sigma-Aldrich, the Netherlands), sodium dodecyl sulfate (SDS, 75746, Sigma-Aldrich, the Netherlands), Span 80 (85548, Sigma-Aldrich, the Netherlands), Tween 80 (P1754, Sigma-Aldrich, the Netherlands), Hexadecyltrimethylammonium bromide (CTAB, H5882, Sigma-Aldrich, the Netherlands), calcium chloride ($\geq$ 97 %, 746495, Sigma-Aldrich, the Netherlands) and sodium chloride ($\geq$ 99 %, Sigma-Aldrich, the Netherlands), were employed to prepare the O/W microemulsions. HCl (0.1 mol/L, 1090601003, Sigma-Aldrich, the Netherlands) and NaOH (97 %, powder, Sigma-Aldrich, the Netherlands) were used for pH adjustment. The citric acid ($\geq$ 99.5 %, powder, Sigma-Aldrich, the Netherlands) was used for membrane cleaning. Demineralized (DI) water was used to prepare the microemulsion, clean the filtration tube, and backwash or forward flush the fouled membranes. Commercial single-channel tubular Al_2O_3 ceramic UF membranes used in the experiments were made of α-Al_2O_3 for both the 600 nm support layer and the selective layer with a maximum pore size of 100 nm (CoorsTek, the Netherlands), where the information on pore size was provided by the membrane manufacturer. The Al_2O_3 membranes chosen for LPCVD had similar permeabilities in the range of 360 to 380 $Lm^{-2} h^{-1} bar^{-1}$. Flat sheet Al_2O_3 membranes with 100 nm pore size were produced by Inopor (Germany) with a rectangular shape (1 cm $\times$ 2 cm) and a thickness of 1 mm. These membranes were coated under the same circumstances as the tubular membranes for contact angle and zeta potential measurements.

2.2. Low-pressure chemical vapor deposition

Dichlorosilane (SiH_2Cl_2) and acetylene (C_2H_2) were used as precursors for the SiC layers deposition. The Al_2O_3 membranes were put on two half wafers, which were located in the center of the LPCVD chamber. The deposition temperature was 860 °C, and the precursors flow ratio (SiH_2Cl_2/C_2H_2) was 6.7 to obtain polycrystalline SiC [29]. The amount of gas flowing into the tube was controlled by mass flow meters with ranges from 0 to 500 standard cm^3/min, and 100 cm^3/min was chosen based on a previous study [29]. The Al_2O_3 membranes without deposition and with deposition times of 10 min, 15 min, 20 min, and 25 min were denoted as H0, H10, H15, H20, and H25, respectively. The 200 nm and 600 nm Al_2O_3 tubular membranes without deposition and with deposition times of 20 min were denoted as H0-200, H0-600, H20-200, and H20-600, respectively.

2.3. Membrane characterization

Scanning electron microscope (SEM) measurements were carried out on a Helios NanoLab 650. In addition, the SEM was attached to an Energy Dispersive X-ray (EDX) spectroscopy (Apollo 40 Silicon Drift Detector, Ametek EDAX^{TSL}) and EDAX Genesis software, which was employed to define the chemical composition of both the pristine Al_2O_3 and LPCVD modified SiC-Al_2O_3 membranes. The Helios Nanolab G3 UC (Thermo Fisher Scientific, USA), which integrates a focused ion beam with an SEM, was used to examine the cross-section of SiC-coated membranes. Using the Focused Ion Beam method, the top thin layers of the SiC-coated sample were removed by directing the gallium ion beam onto it, sequentially revealing a new cross-section. This newly exposed surface was then visualized using the electron beam of an SEM. XRD (X-ray Diffraction) was conducted with an X-ray diffractometer (D8-Discover, Bruker, USA) and Eiger-2 500k 2D-detector to measure the SiC crystal structure. Surface roughness measurements were performed by atomic force microscopy (AFM) (Dimension Icon, Bruker, USA) in tapping mode in the air. The Gwyddion software was used to analyze the AFM images and provide quantitative roughness data. Transmission electron microscopy (TEM) images were collected using a Titan aberration-corrected transmission electron microscope (Thermos Fisher, FEI company).

The water contact angle (WCA) and underwater oil contact angle (UOCA) of the pristine Al_2O_3 membranes and the LPCVD-modified SiC-Al_2O_3 UF membranes were performed by a contact angle instrument with a manual adjustable zoom lens (Dataphysics OCA25, Germany). The WCA measurements, conducted on a minimum of three times at distinct locations of each membrane, were measured by dosing 2 μL water on the membrane surface. The UOCA measurements were conducted using captive bubble mode, where a droplet of soybean oil was captured by the bent dosing needle (SNC 050/026, Benelux Scientific BV, the Netherlands) under the membrane holder (SHC 20, Benelux Scientific BV, the Netherlands), which fixed the commercial flat Al_2O_3 and SiC-coated Al_2O_3 membrane in the aqueous phase in a glass cell (GC 50, Benelux Scientific BV, the Netherlands).

The zeta potential was used to estimate the surface charge of the membranes using an electrokinetic analyzer (SurPASS, Anton Paar, Graz, Austria). The instrument measured the streaming current coefficient, and the Helmholtz–Smoluchowski equation was used for the calculation of the zeta potential of the flat membrane. The isoelectric point (IEP) was measured in a titration system, encompassing a pH range of 3 to 10 with a pH interval of 1. Three-point bending tests were performed, using a mechanical testing system (ElectroPuls E20000, Instron, USA), to measure the bending strength of the membranes. The capillary flow porometry (Porolux 500, IBFT GmbH, Germany) was employed to measure the bubble point, mean pore size, and pore size distribution of the membranes. The pore size distribution was calculated based on the Young-Laplace equation (Eq. (1)) [30]:

$$D = \frac{4\gamma \bullet cos\theta}{P} \tag{1}$$

Where D is the effective diameter of membrane pores (m), γ is the surface tension of the wetting liquid (0.016 N/m), θ is the contact angle at the fluid and membrane surface interface (0°), and P is the applied pressure (N/m^2).

2.4. Oil-in-water microemulsions

Various nano-sized O/W emulsions, namely non-ionic Tween 80-stabilized microemulsion, anionic SDS-stabilized microemulsion, and cationic CTAB-stabilized microemulsion, all in combination with co-surfactant Span 80, were prepared for membrane filtration experiments, to study the impact of the charge of the emulsions on fouling of the membranes, respectively. To obtain 500 mg/L Tween-80 stabilized microemulsion, 2 g Soybean oil, 0.2 g Span 80, and 0.2 g Tween 80 with a mass ratio of 10:1:1 were added into 1 L DI water (pH = 5.6), followed by continuously high speed stirring at 2000 rpm with a magnetic stirrer (L32, LABINCO, the Netherlands) for one day and ultrasonication in a sonifier (3800, Branson, USA) for one day, in accordance with previous studies [1,31,32]. Prior to each experiment, the preparation of the fresh emulsion involved the dilution of 1 L O/W microemulsion with 4 L DI water to a constant oil concentration of 500 mg/L since 50–1000 mg/L oil and grease content are typically present in oily wastewater [12]. The same procedures were used for the SDS and CTAB-based
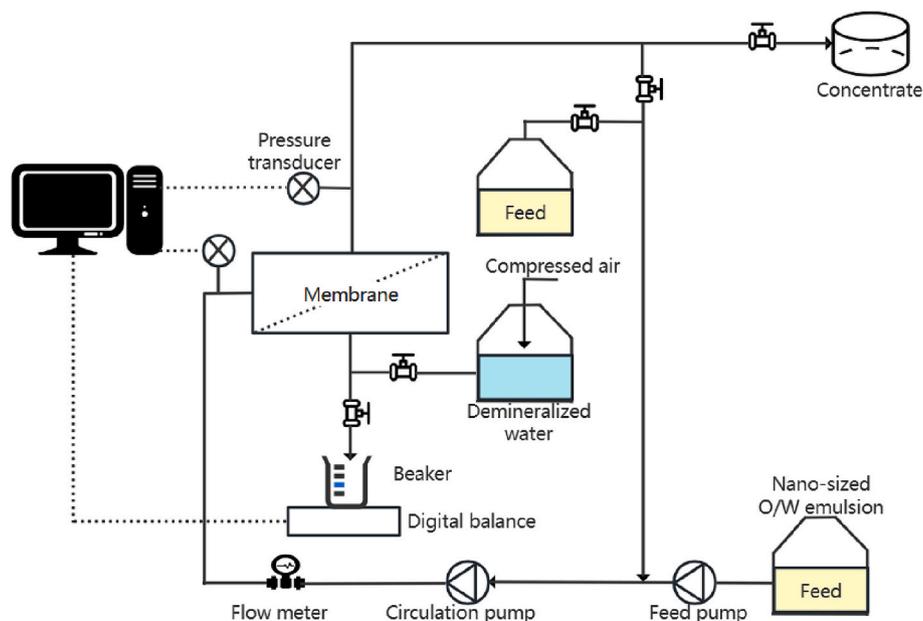
Fig. 1. Schematic diagram of constant flux filtration system.

microemulsions. 1 mM NaCl were added to the microemulsion to adjust the ionic strength. The pH of the microemulsions was measured by a pH meter (228HTE, PCE Brookhuis B.V., the Netherlands). The sizes and size distributions of the oil droplets were measured with a particle size analyzer (Bluewave, Microtrac, USA), while the zeta potential of the microemulsions was obtained using a Malvern Zetasizer Nano instrument (ZS90, Malvern, UK). The stability of the microemulsions were confirmed by similar oil droplet size distribution after the emulsions were left to stand for 1 day and 7 days (Fig.S14).

2.5. Determination of threshold flux

The conventional flux stepping method was employed to estimate the threshold flux [33,34]. This method involved incrementally increasing the permeate flux while simultaneously recording the transmembrane pressure (TMP) for each step. The threshold flux was determined by using the average TMP (TMP$_{avg}$). The flux stepping tests use a range of fluxes varying from 40 Lm^{-2} h^{-1} to 100 Lm^{-2} h^{-1}. Each step in the test lasted for 20 min, with intervals of 10 Lm^{-2} h^{-1}.

2.6. Fouling experiments with microemulsions

2.6.1. Fouling experiments with constant permeate flux

Microemulsion filtration experiments were carried out with a constant permeate flux crossflow setup (Fig. 1). The concentrate stream was discharged back into the feed during filtration, while a steady flow was provided by the digital diaphragm metering pump (DDA17-7, Grundfos, Denmark). The gear pump (VGS Standard, Verder Liquids, the Netherlands), employed as a circulation pump, was utilized to maintain a consistent crossflow velocity (CFV) of 0.59 m/s. The TMP was calculated by averaging the inflow and outflow pressures on both sides of the membrane module. To avoid a discrepancy between the feed pump flow and the permeate flux, a digital balance (FZ-3000iWP, Japan) was utilized to measure the weight of the permeate, and then it was converted to permeate flux.

2.6.2. Filtration protocol

Each filtration experiment began with a pure water permeance test in a crossflow mode, using the same permeate flux and crossflow used for microemulsion filtration. The fouling experiments for the SiC-coated membranes with different deposition times comprised multiple cycles,

which were reliant upon the microemulsions properties (pH and surfactant type). Each filtration cycle consisted of three stages: (i) filtering the microemulsions at a specified flux for 20 min; (ii) backwashing to remove reversible fouling at a constant backwash flux of 1080 Lm^{-2} h^{-1}; (iii) forward flushing with microemulsion for 10 s at a CFV of 0.59 m/s to drain the concentrated water. To have a fair comparison of backwash efficacy, due to the decreased permeance of the SiC-coated membranes, the fouled H0, H10, H15, H20, and H25 membranes were backwashed for 1 min with DI water at pressures of 3 bar, 3.375 bar, 3.857 bar, 4.5 bar, 5.4 bar, 6.75 bar, respectively to obtain the same backwash flux in every membrane. Every experiment was conducted in duplicate.

2.6.3. Data analysis

Permeate fluxes and water temperature were measured at 10-s intervals. The pure water permeance was assessed by filtering DI water at 5 bar. This preliminary step was conducted to verify the thorough cleaning of the membranes prior to the start of the experiments using Eq. (2) [35]:

$$L_{P,20°C} = \frac{J \bullet e^{-0.0239 \bullet (T-20)}}{\Delta P} \qquad (2)$$

Where $L_{p,20\ °C}$ represents the water permeance at 20 °C (Lm^{-2} h^{-1} bar^{-1}), J denotes the membrane flux (Lm^{-2} h^{-1}), and T denotes the water temperature (°C).

The relation between the permeate flux, TMP, viscosity, and membrane resistance is shown in Eq. (3):

$$J = \frac{TMP}{\mu R} \qquad (3)$$

Where R represents the resistance to mass transfer (m^{-1}), μ denotes the permeate viscosity (Pa·s), and J denotes the permeate flux through the membranes (m/s). The calculation of the membrane resistance is based on the resistance-in-series model [36,37].

$$TMP_{Normalized} = \frac{TMP}{TMP_0} \qquad (4)$$

The normalized TMP is the ratio of TMP divided by TMP$_0$, as shown in Eq. (4). The TMP$_0$ is the TMP corresponding to the required flux (80 Lm^{-2} h^{-1}) with a clean membrane.

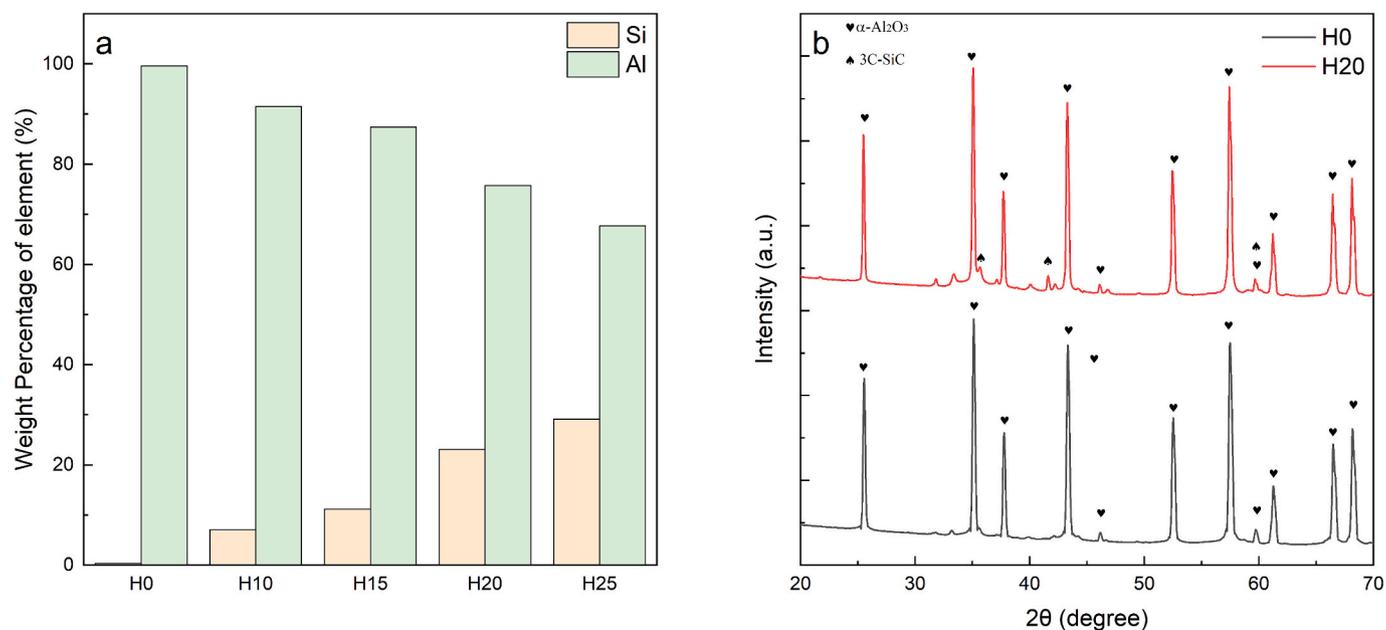The methods used to determine oil and chemical oxygen demand

Fig. 2. (a) Weight percent of element for the H0, H10, H15, H20, and H25 membranes. (b) XRD patterns of the H0 and H20 membranes.
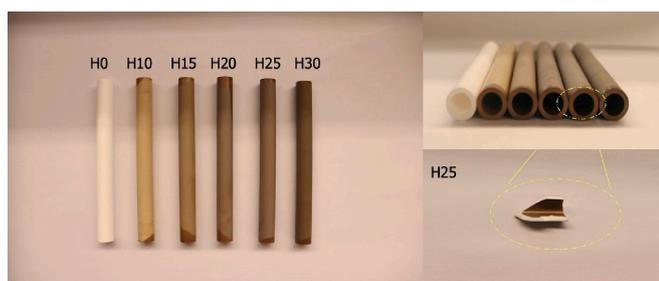

Fig. 3. Photographs of the Al_2O_3 (H0) membrane and SiC-coated Al_2O_3 (H10, H15, H20, H25) membranes.

(COD) rejection are provided in the supporting information, as shown in Fig.S16 and S17.

3. Results and discussion

3.1. Membrane morphology

EDX spectroscopy analyses were conducted to probe and verify the elemental compositions of the Al_2O_3 membranes and SiC-coated Al_2O_3 membranes. The main composition of the SiC membrane, C and Si, was confirmed by the two strong peaks at 0.277 keV and 1.739 keV, respectively (see Fig. S1). As shown in Fig. 2a, with the increase in deposition time from 0 min (without deposition) to 25 min, the weight percentages of Si increased from 0 to 25.09 wt%, while the weight percentages of Al decreased from 89.96 to 61.03 wt%. EDX mapping distribution analysis, as shown in Fig. S2, confirms these observations.
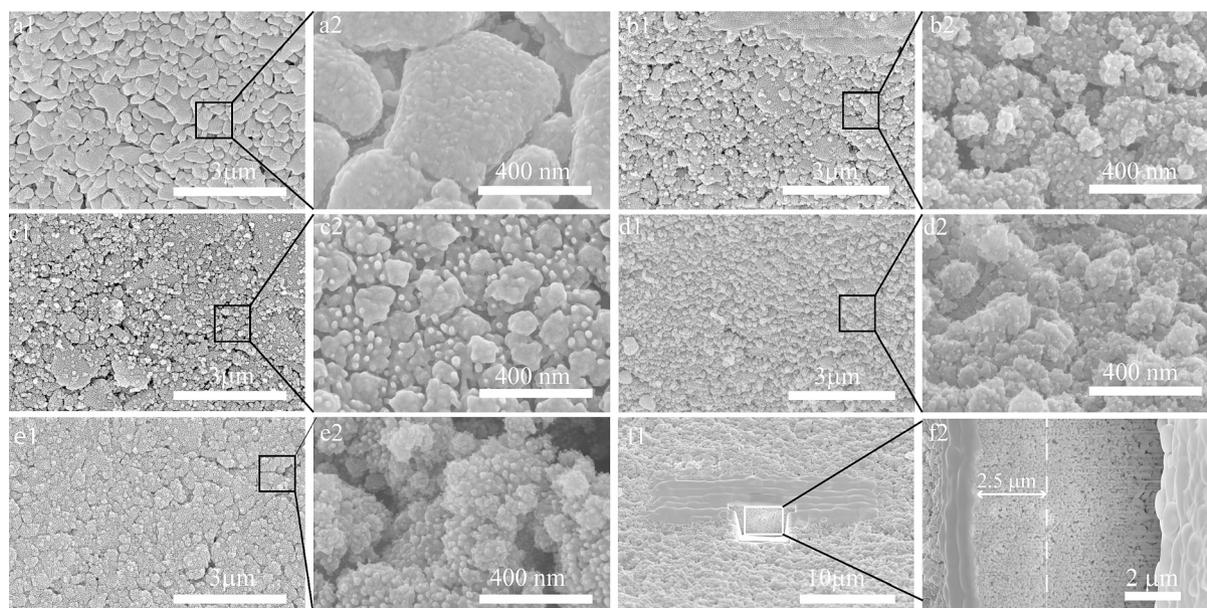

Fig. 4. SEM images for the surface of the (a) H0 and (b) H10, (c) H15, (d) H20, (e) H25 membranes, and (f) the cross-section of the H20 membrane.
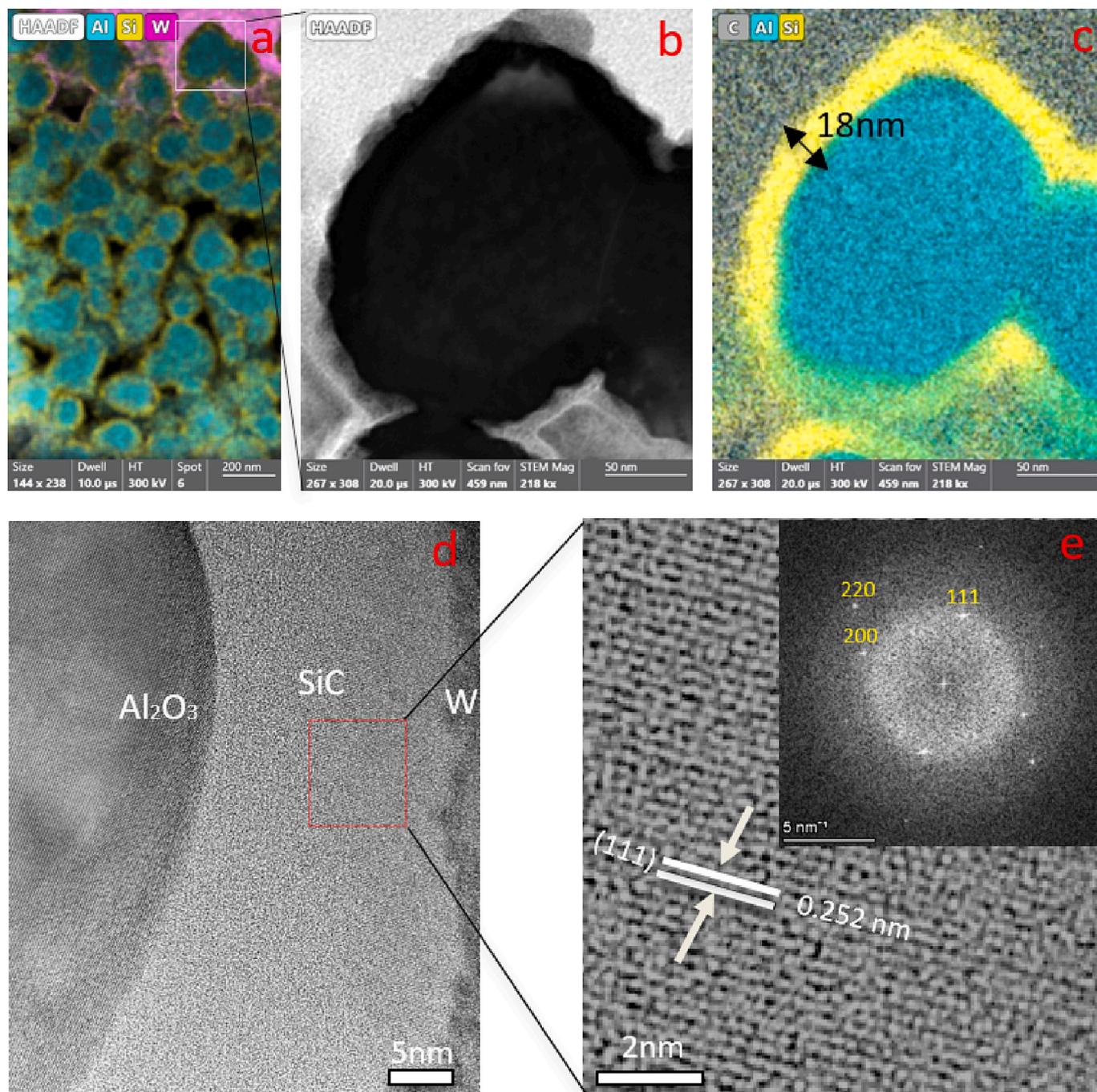
Fig. 5. (a) STEM EDX net intensity maps of the cross section of the H20 membrane. (b) STEM images and (c) EDX net intensity maps of a SiC coated alumina particle near the top. (d) and (e) High-resolution TEM images of the H20 membrane with SAED patterns (upper right).

Fig. 2b shows the XRD patterns of the H0 and the H20 membrane. The upper spectrum (red line) shows the characteristic XRD pattern of the polycrystalline layer for the H20 membrane, and the main phase identified is 3C-SiC polytype with diffraction peaks at 35.61°, 41.4° and 60°, respectively, ascribed to (111), (200), (220) diffraction planes of the beta phase SiC.

An SEM was employed to examine further the surface and cross-section structure of the Al_2O_3 membrane and SiC-coated Al_2O_3 membranes. The separation layer of the membranes was in the range of 24 to 30 μm (Fig. S3). Fig. 3 shows one pristine Al_2O_3 membrane and SiC-coated membranes with various deposition times. SiC has been deposited on both sides of the membranes. The deposition on the support layer did not affect the membrane's permeability due to the relatively small layer thickness of SiC compared to the pore size of the support layer, as evidenced by the SEM image in Fig. S20. With the increased deposition time, the color changed from white to golden and dark grey, and SiC nanoparticles aggregated on the Al_2O_3 surface, leading to the formation of pronounced nano-scale protrusions (Fig. 4) [38]. With the deposition time further increased to 25 min, nanoparticles of larger sizes were observed. To evaluate the coating depth of SiC, a combination of the focused ion beam and SEM was applied to obtain high-resolution SEM images of the cross-section of the H20 membrane, as depicted in Fig. 4f. The results showed that the deposition mainly happened on the surface (2.5 μm) at the deposition time of 20 min, which was confirmed by the results of SEM-EDAX line scan (Fig. S3f and Fig.S15 a-c). These scans indicated that the Si intensity stayed constant, and higher than the
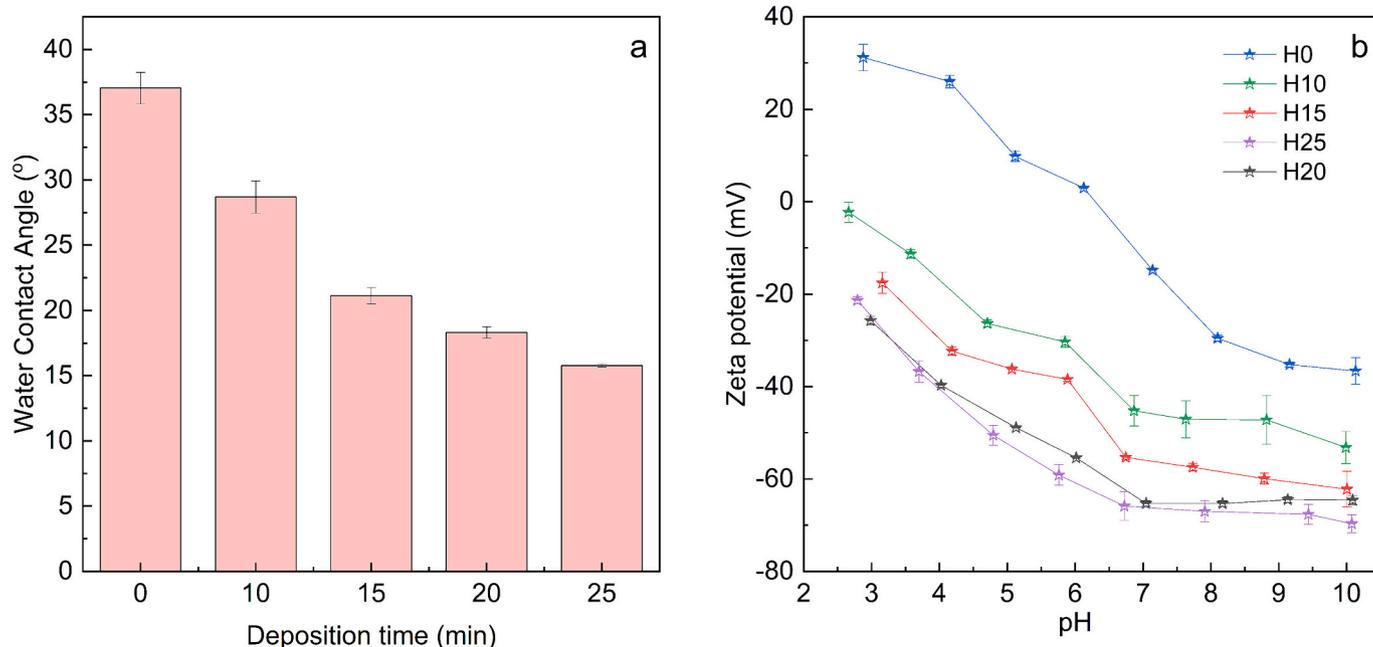
Fig. 6. Initial water contact angle (a) and zeta potential (b) of Al_2O_3 membrane (H0) and SiC-coated Al_2O_3 membranes (H10, H15, H20, H25) with increasing deposition times.

background noise, over the entire separation layer, indicating adequate infiltration of the precursors into the membrane, where the penetration depth of SiC was around 2.5 μm.

Fig. 5 shows the thickness of the uniform SiC layer on the surface of the Al_2O_3 particles for the H20 membrane, observed by TEM, being 18 ± 1 nm. The interface between the Al_2O_3 particles and SiC coating layer is clearly visible. Besides, high-resolution TEM images show an amorphous SiC layer with some 5–10 nm crystalline 3C-SiC (β-SiC) particles. A laminated structure, embedded in the amorphous SiC matrix, confirmed the presence of the 3C-SiC polytype (Fig. 5d). The lattice plane distances were 2.517, 2.180, 1.541 Å, respectively, corresponding to the {111}, {002} and {022} planes of 3C-SiC (Fig. 5e). This finding is in accordance with the XRD results, described in previous section.

The membrane surface morphology was also studied by AFM, and the results are shown in Fig. S5. The average surface roughness (R_a) and the root-mean-square surface roughness (R_q) values of the Al_2O_3 membrane (Fig. S5a) were 55 ± 3 nm and 43 ± 4 nm, respectively, illustrating a relatively smooth surface. With the increase in deposition time, from 10 min to 25 min, the R_a increased from 66 ± 1 nm to 82 ± 2 nm (Fig. S5b-e), respectively, indicating that the deposition of SiC nanoparticles provided an increase in roughness of the membrane surface. The increase of R_a could be explained by the increase in the size of the SiC nanoparticles, which covered the Al_2O_3 particles, as also illustrated by the SEM images (Fig. 4), which is consistent with the work of Lin et al. [39]. Increased surface roughness contributes to a rise in turbulence, and oil droplets could gain momentum to slip away from the pores, leading to less fouling [40]. In addition, the relationship between the size of the oil droplet and the characteristic length of roughness also influences fouling since the underwater superoleophobicity of the coated membranes reduces fouling if the size of oil droplets exceeds the characteristic length [41].

3.2. Membrane hydrophilicity and zeta potential

The effectiveness of membranes for oil/water separation is significantly influenced by surface wettability. Membranes with hydrophilic surface (WCA < 90°) are underwater oleophobic or even superoleophobic when the UOCA is >150° [42]. All SiC-deposited Al_2O_3 membranes (H10, H15, H20, H25) were in-air hydrophilic (Fig. 6a and

Fig. S6) and underwater superoleophobic (Fig. S7). These properties can be attributed to a significant number of hydroxyl groups on the SiC-deposited Al_2O_3 membrane surface [21], which is essential for their oil fouling resistance. Due to the porous structure of H10, H15, H20, and H25, a static WCA measurement was impossible since all the water drops were easily dispersed on the membrane surface and rapidly infiltrated into the pores. Fig. S8 shows the real-time, dynamic WCA of the membranes, indicating that the WCA of the Al_2O_3 membranes decreased from 36° to <5° within 2.8 s, while for the SiC-coated membranes, the WCA rapidly declined to <5° within 1 s. Therefore, only the initial WCA was determined, being 37° ± 1.2° for the Al_2O_3 membrane and 29° ± 1.2° to 21° ± 0.6°, 18° ± 0.3° and 15° ± 0.1° for the H10, H15, H20 and H25 membrane, respectively. This is consistent with a previous study where the WCA of SiC hollow fiber membranes is 11.3° [13]. In addition, according to Wenzel's equation, increasing the roughness of hydrophilic surfaces enhances their hydrophilicity [43], which is consistent with our finding that the surface roughness increased with deposition time. Besides, the UOCA of H0 and H20 were 137° and 168°, respectively. This indicates the underwater oleophobicity was increased with the deposition of the SiC layer. Soybean oil adhered to the Al_2O_3 underwater membrane surface, while the soybean oil droplets remained spherical for the SiC-coated membrane, and no evident oil adhesion after pulling down the oil droplet from the SiC-coated surface was observed, as shown in Fig. S9. These observations indicate the improved hydrophilicity and superoleophobicity of the membranes after SiC deposition.

The zeta potential of the membrane is an indication of the surface charge, and, for a specific surface, it is usually dependent, amongst others, on the pH. Usually, the membrane surface becomes more negatively charged with an increase in pH [9]. Fig. 6b shows that the zeta potential of membranes indeed decreased with an increase in pH and that the IEP of the Al_2O_3 membranes became 6.4, which is consistent with the results reported by Nagasawa et al. [26]. Besides, all SiC-coated membranes were negatively charged in the measured pH range (3–10) and were more negatively charged compared with the Al_2O_3 membranes. The zeta potentials of the H20 and H25 membranes showed similarities but were lower than those of the H0, H10, and H15 membranes. A possible explanation is that the SiC layer is not closed at lower deposition time, and all the alumina is covered by SiC after 20 min of deposition [44].
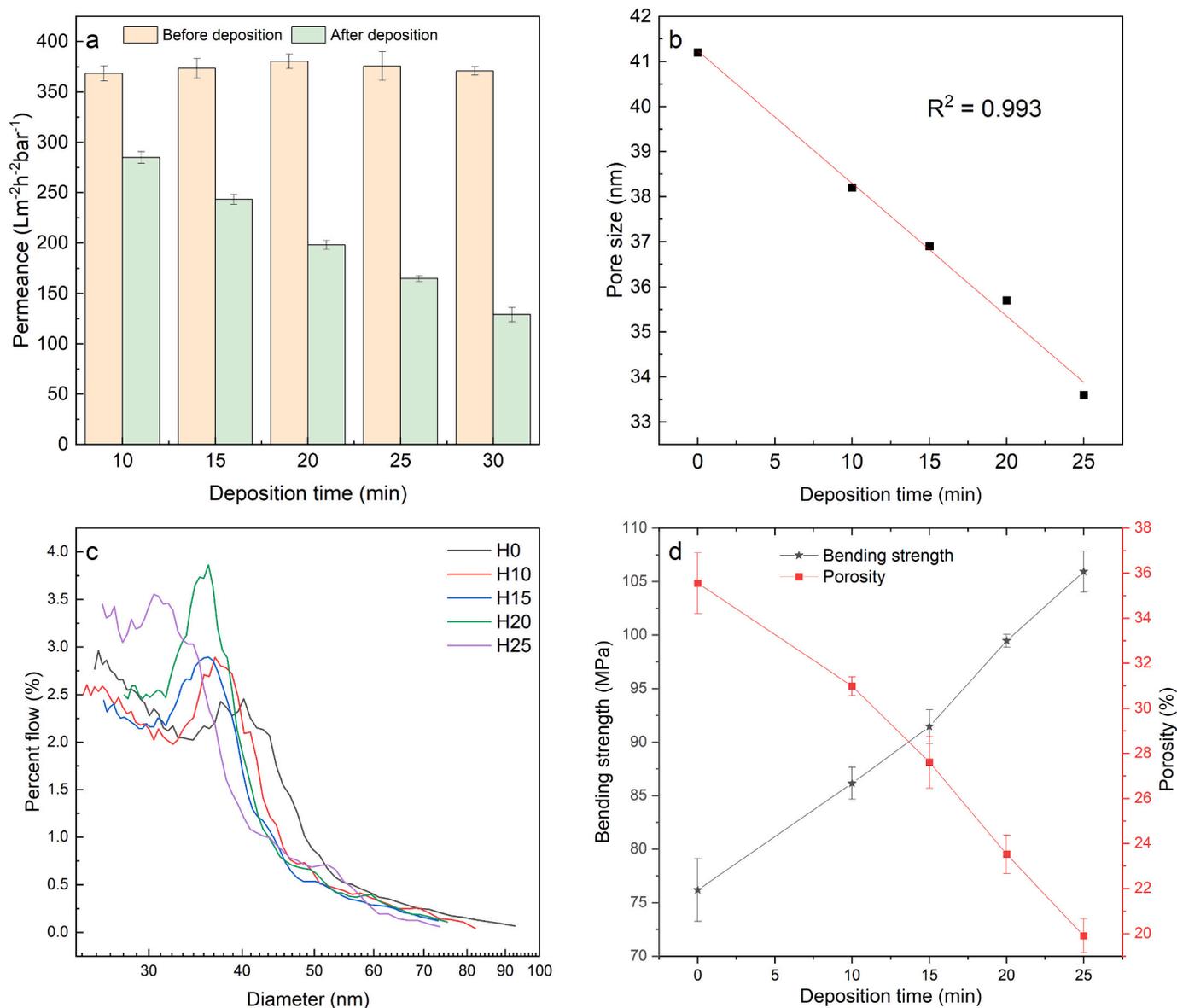
Fig. 7. (a) Permeance, (b) pore size, (c) pore size distribution, and (d) bending strength and porosity of the Al_2O_3 membrane (H0), and the SiC-coated Al_2O_3 membranes with increasing deposition times: H10, H15, H20, H25.

From Table S2, it can be observed that the pH value had little impact on the zeta potential of the oil droplets, which is in accordance with previous studies, where it has been reported that the pH of the solution does not have an effect on the surface charge of emulsions stabilized with ionic surfactants due to the strong acid sulfonate heads of surfactant [45].

3.3. Pure water permeance, membrane pore size and oil rejection

Pure water permeance tests were carried out, and the results are depicted in Fig. 7a. The permeance of the membranes exhibited a linear reduction, ranging from 368 ± 8 to 165 ± 3 Lm^{-2} h^{-1} bar^{-1}, respectively, as the deposition time increased from 0 min (no deposition) to 25 min. This can be explained by the linear decrease of the mean membrane pore size, from 41.2 nm (H0) to 33.6 nm (H25), respectively (Fig. 7b). The bubble point diameter, which reflects the maximum pore size of the membrane, also showed a decrease with an increase in deposition time from 93 nm (H0) to 73 nm (H25), respectively (Fig. 7c). Therefore, the rejections of the nano-sized oil droplets (104 nm) of both the Al_2O_3 membrane and SiC-coated membranes were over 99 % due to the size-

sieving effect (Fig. S10), as indicated by Zhang et al. [46]. Additionally, the small oil droplets could potentially be trapped within the irregular channels of the membrane support. However, the COD rejection (98 ± 0.4 %) was lower than the oil rejection, probably because the small surfactant molecules can pass through the membrane pores. In the meantime, the porosity of the membranes dropped linearly with the increase in the SiC deposition time. According to data gathered through Image J analysis of the SEM images (Fig. 7d and Fig. S4), the porosity decreased to 19.9 % when the deposition time was increased to 25 min. The decreased porosity, improved grain bonding (Fig. S18) and deposition of the SiC on the defects of the H0 membrane surface (Fig. S19) contributed to the improved bending strength from 76 ± 9 MPa to 106 ± 10 MPa of the H0 membrane and H25 membrane, respectively (Fig. 7d).

3.4. Comparison of fouling of the various membranes

Fig. 8 shows the comparison of the fouling of the Al_2O_3 membrane (H0) and the four SiC- Al_2O_3 membranes (H10, H15, H20, H25) for microemulsion filtration at a constant flux of 80 Lm^{-2} h^{-1}, respectively.
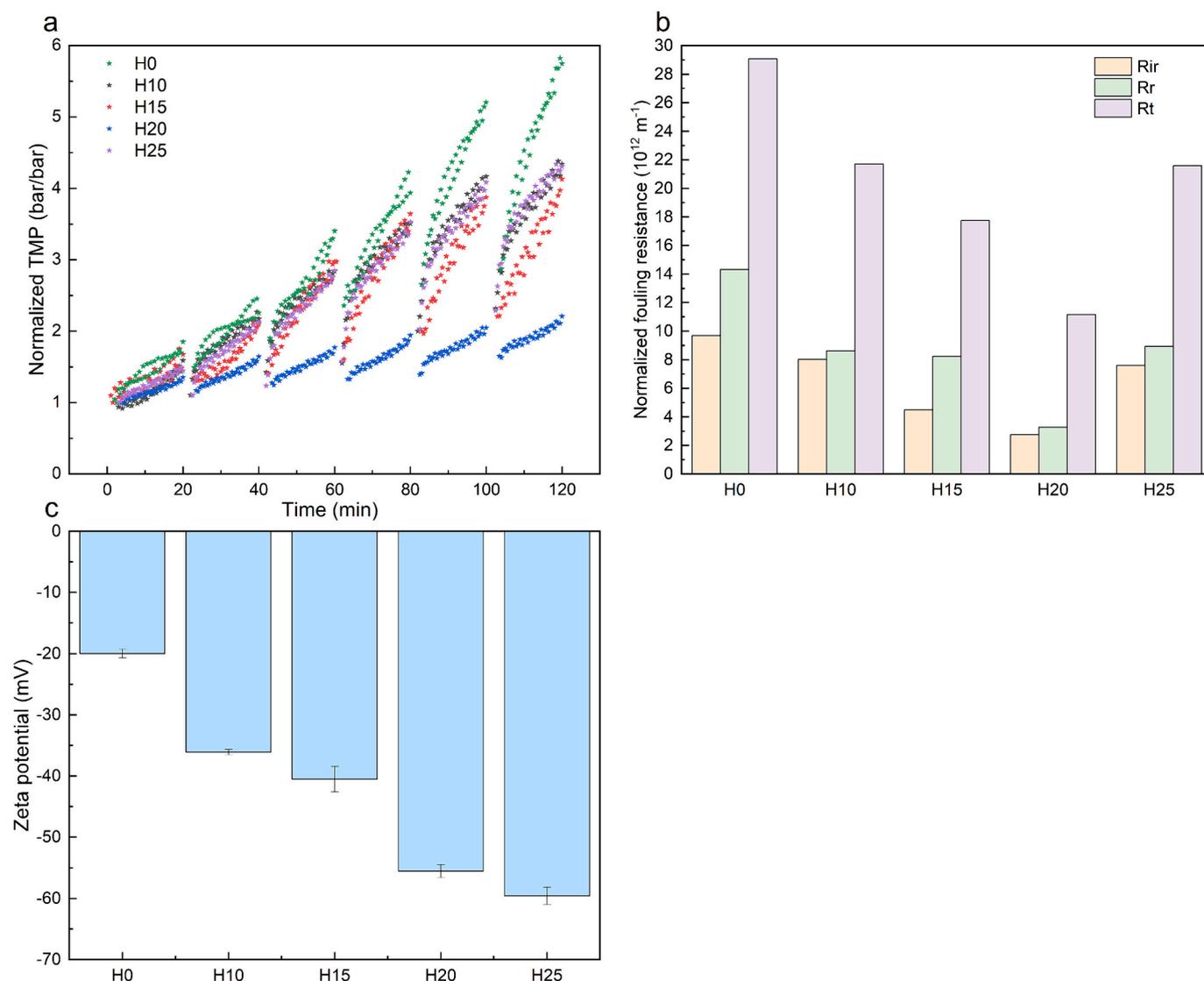
Fig. 8. The normalized (a) TMP and (b) fouling resistance of the H0, the H10, the H15, the H20, the H25 membrane for the filtration of microemulsion (500 mg/ L soybean oil with 50 mg/ L Span 80 and 50 mg/L Tween 80) ; (c) is the zeta potential of the H0 the H10, the H15 the H20, the H25 membranes in the surfactant solution with 50 mg/ L Span 80 and 50 mg/L Tween 80.

This flux was selected based on the threshold fluxes of the H0 membrane ($76\ Lm^{-2}\ h^{-1}$) and the H20 membrane ($86\ Lm^{-2}\ h^{-1}$) (Fig. S11). The normalized TMP curve (Fig. 8a) shows that the H0 membrane showed the greatest fouling tendency. However, it is worth noting that the normalized TMP curves showed similarities across all membranes in the initial cycles. Following the initial cycle, the backwash was effective, indicating little irreversible fouling. However, with an increasing number of filtration cycles, irreversible fouling gradually accumulated, causing a more rapid increase in TMP.

The fouling resistance was also used to calculate the reversible and irreversible fouling. Fig. 8b illustrates the fouling resistance observed in the six cycles for all membranes. Both irreversible fouling and reversible fouling decreased with the increase in deposition time until 20 min. The R_r and R_{ir} were reduced by 77 % and 72 %, from 14.31×10^{12} to $3.29 \times 10^{12}\ m^{-1}$ and from 9.69×10^{12} to $2.76 \times 10^{12}\ m^{-1}$, respectively, as the deposition time increased to 20 min. However, more fouling was noticed for the H25 membrane, probably due to the lower permeance and smaller pore size, resulting in higher TMPs at constant flux and, thus, more accumulation of irreversible fouling [47].

With the increase in deposition time, the membranes became more hydrophilic and more negatively charged (Fig. 6). Both electrostatic

interactions and hydrophilic interactions affect the membrane fouling in crossflow filtration [48]. The pH of the microemulsion was 5.6 and, at this pH, the zeta potentials of the H0, H10, H15, H20, H25 membranes (Fig. 7c) were − 20.0 mV, −30 mV, −38 mV, −55.5 mV and -59.6 mV, respectively. This means that the surface of all the membranes was negatively charged. The microemulsions stabilized by Tween 80 and Span 80 were slightly negatively charged (-21.30 ± 0.73 mV) due to the deprotonation of the hydroxyl groups present in Tween 80 [49]. Therefore, weak electrostatic repulsion between the nano-sized oil droplets and the Al_2O_3 membrane surface led to an increased fouling potential, whereas stronger electrostatic repulsion forces occurred for SiC-coated membranes. This observation is consistent with the results obtained with the filtration of negatively charged oil droplets over a negatively charged ZrO_2/TiO_2 membrane, leading to a decrease in cake layer formation and the accumulation of fouling [50]. Probably, the hydrophilicity of the membranes, which improved after SiC deposition (Fig. 6a), also prevented the membrane from adsorbing or depositing oil. It has also been reported that the improved hydrophilicity of isotropic PES membrane leads to less fouling due to decreased oil layer formation [24].
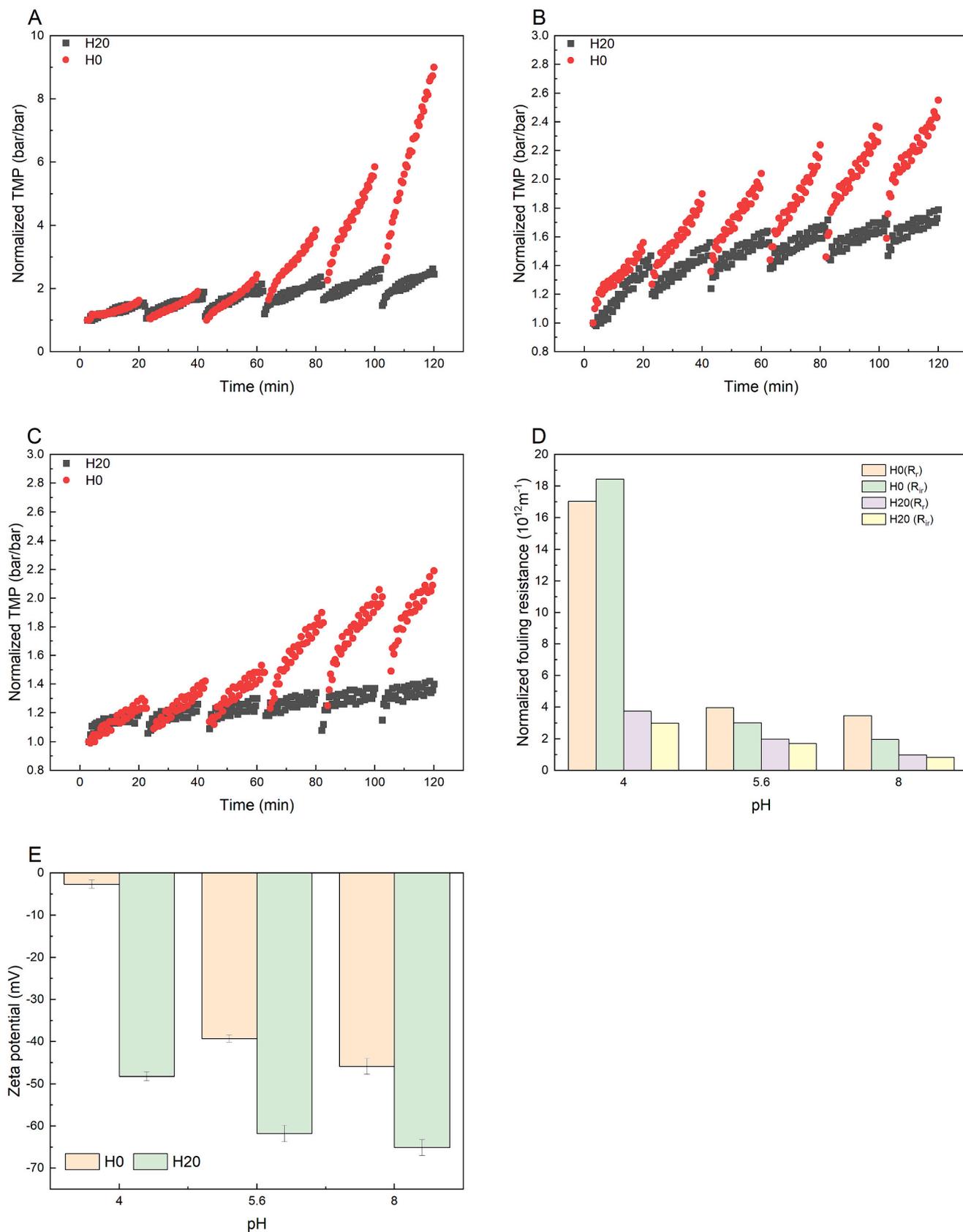
Fig. 9. Normalized TMP of the H0 and the H20 membrane or the filtration of microemulsion stabilized with 50 mg/L Span 80 and 50 mg/L SDS at the pH of (a) 4, (b) 5.6, and (c) 8; (d) is the normalized fouling resistance of the H0 and the H20 membrane at the pH of 4, 5.6 and 8; (e) is the zeta potential of the H0 and the H20 membrane at the pH of 4, 5.6 and 8.
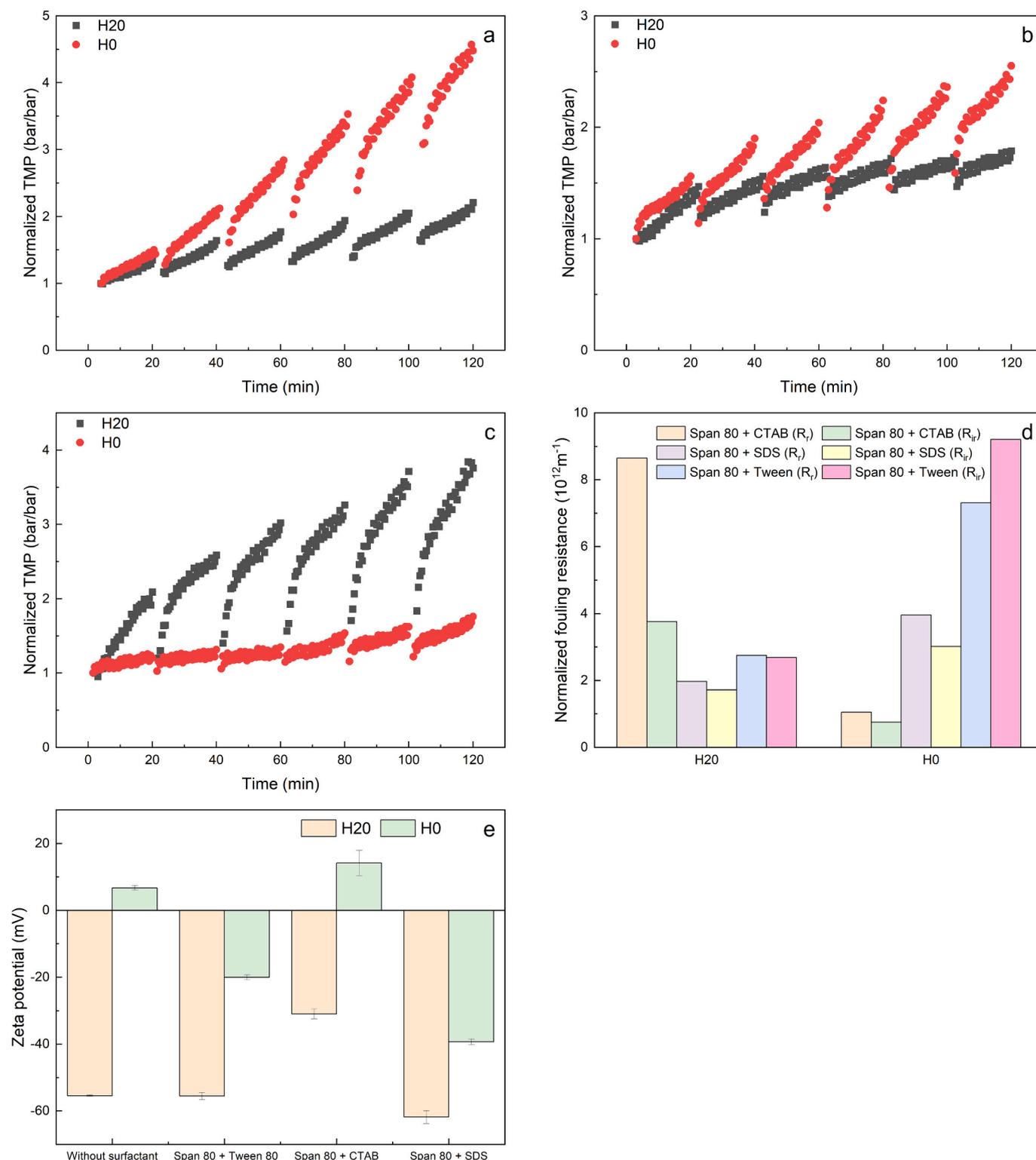
Fig. 10. Fouling comparison of the H0 and the H20 membrane during the filtration of microemulsions stabilized with various types of surfactant: 50 mg/L Span and 50 mg/L (a) Tween 80, (b) SDS, (c) CTAB. (d) is the normalized fouling resistance of the H0 and H20 membranes at various surfactant types. (e) is the zeta potential of the H0 and the H20 membrane in different surfactant solutions.

3.5. Fouling behavior at various pHs, surfactants and pore sizes

3.5.1. Fouling behavior at various pHs

To investigate the influence of pH on the fouling of the H0 and the H20 membrane, three different pH values (4, 5.6, and 8) were selected. The normalized TMP of H0 and H20 are shown in Fig. 9, which reveals

that with an increase in pH of the microemulsion, the performance of both the H0 and the H20 membranes improved, while the fouling was more severe in the H0 membrane compared to the H20 membrane at the same pH. This phenomenon can be ascribed to the fact that as the pH rises, the surface charge of the membrane becomes increasingly negative [51]. The zeta potential of the H20 membrane, e.g., experienced a
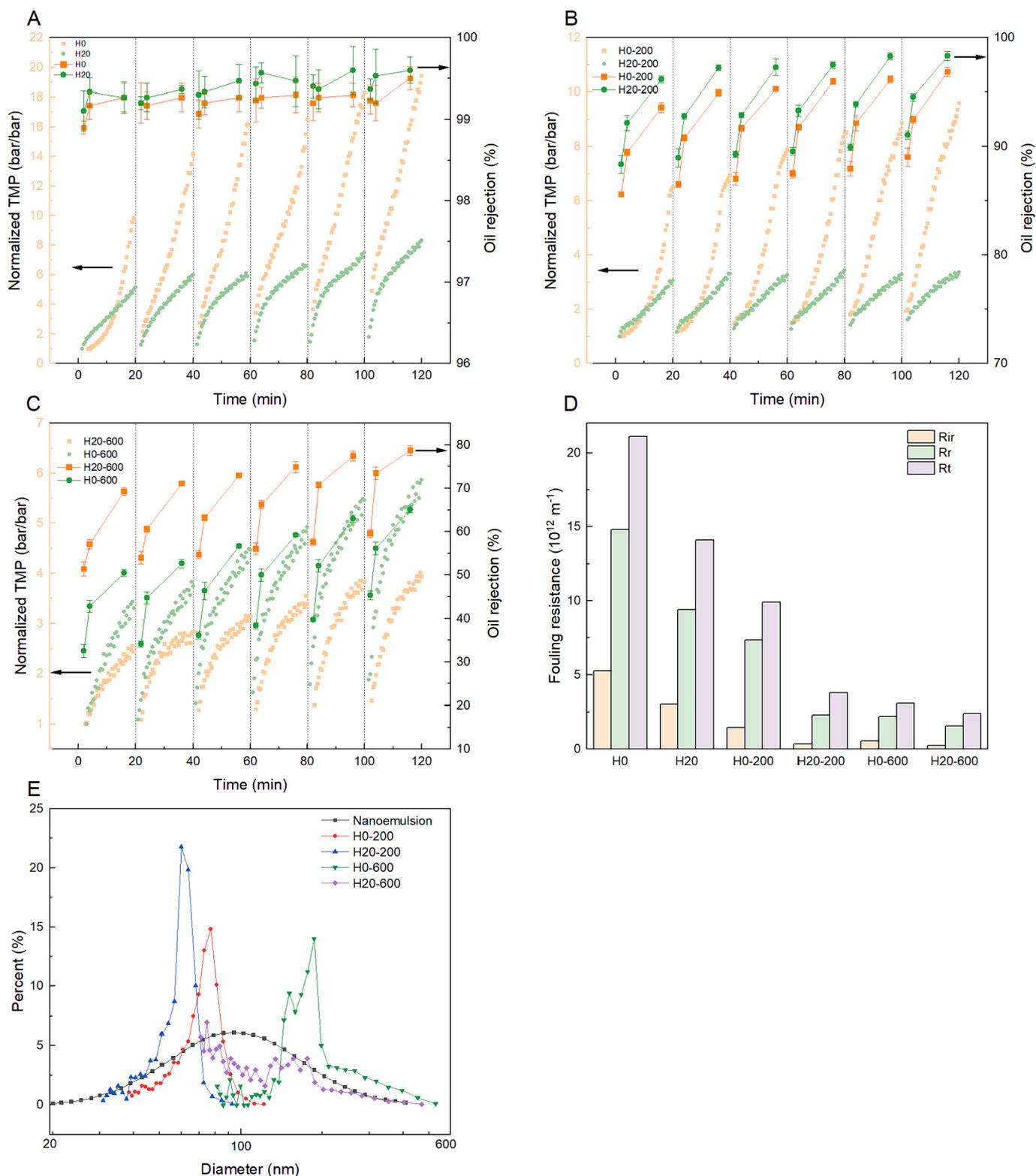
Fig. 11. Fouling comparison of (a) the H0 and the H20 membrane, (b) the H0–200 and the H20–200 membrane, (c) the H0-600 and the H20-600 membrane during the filtration of microemulsions stabilized with 50 mg/L Span 80 and 50 mg/L Tween 80 at the salinity of 1 mM. (d) is the normalized fouling resistance of the membranes at various pore sizes. (e) is the pore size distribution of the membranes and particle size distribution of the microemulsions stabilized with 50 mg/L Span 80 and 50 mg/L Tween 80 at the salinity of 1 mM.

reduction from −48.2 mV to −65.1 mV as a result of a rise in pH from 4 to 8, respectively, while the zeta potential of microemulsions remained constant with the change in pH, as shown in Table. S2. At a pH of 5.6, the H20 membrane (−61.8 mV) would repulse oil droplets more strongly.

Therefore, the H20 membrane would retain oil droplets on the surface and showed less susceptibility to fouling by negatively charged oil droplets. However, the surface charge of the H0 membrane was less negative (−39.2 mV), as can be seen from Fig. 9e, compared with the

H20 membrane, leading to more fouling. When filtering the microemulsion at a pH of 8, the zeta potential of the H0 membrane was further decreased to −45.8 mV, and the electrostatic repulsion enhanced and decreased fouling. The zeta potential value of the H20 (−65.1 mV) was nearly 1.5 times lower than that of the H0 (−45.8 mV). Thus, a higher electrostatic repulsion existed, which supports the results of better fouling resistance of H20 at a pH of 8.

With the increase in pH, stronger repulsive electrostatic interactions led to the accumulation of oil droplets above the membrane surface and formed a cake layer [48]. Therefore, it became more difficult for the oil droplets to squeeze and enter the pores, and thus, less irreversible fouling existed. Fig. 9d shows a reduction in the R_r and R_{ir} of H0, specifically, from 7.04×10^{12} to 3.46×10^{12} m^{-1} and from 18.43×10^{12} to 1.97×10^{12} m^{-1}, respectively, when the pH climbed from 4 to 8. Nevertheless, the R_r and R_{ir} of H20 exhibited a moderate drop, from 3.74×10^{12} to 0.98×10^{12} m^{-1} and from 3.00×10^{12} to 0.83×10^{12} m^{-1}, respectively.

3.5.2. Fouling behavior with various surfactant types

The stability of O/W microemulsions depends on the surfactants present in oily wastewater. The type of surfactant has a significant effect on membrane fouling since the colloidal surface charge strongly influences fouling [14,26,49,52]. Microemulsions with combinations of surfactant Span 80 with three different surfactants, Tween 80, SDS and CTAB, respectively, had similar oil droplet average sizes as shown in Table. S1 and Fig. S12, being 99, 108 and 123 nm, respectively.

To investigate the impact of free surfactant molecules on the fouling of the membranes, a series of ultrafiltration (UF) experiments were carried out using pure Span 80 and Tween 80, SDS, CTAB (50 mg/L) in DI water (Fig. S13). The results showed that TMPs remained constant, and no fouling occurred since no micelles formed, and the small surfactant molecules could pass through the membrane pore and go into a permeate solution. As shown in Fig. 10e, the zeta potentials of both the H0 and the H20 membrane followed the order: Span 80 + CTAB > Span 80 + Tween 80 > Span 80 + SDS (H20: −30.9 ± 1.4, −55.5 ± 1.1, −61.8 ± 1.9 mV, respectively; H0: 14.1 ± 3.8, −20.0 ± 0.7, −39.3 ± 0.8 mV, respectively). As depicted in Fig. 10a,e and Table S2, the H20 membrane filtering the microemulsion stabilized with Span 80 and Tween 80 (−21.30 ± 0.73 mV) showed a lower fouling tendency than the H0 membrane due to a more negatively charged surface of the H20 membrane (−55.5 ± 1.1 mV) than that of the H0 membrane (−20.0 ± 0.7 mV).

Similarly, as depicted in Fig. 10b,e and Table S2, the microemulsion stabilized with Span 80 and SDS (−58.3 ± 0.82 mV), the H0 membrane showed a higher fouling tendency and (ir)reversible fouling than the H20 membrane (Fig. 10d), due to weaker electrostatic repulsion between oil droplets and the negatively charged H0 membrane's surface (−39.3 ± 0.8 mV) than that of the H20 membrane's surface (−61.8 ± 1.9 mV). The H0 membrane surface charge changed from highly positive to slightly/moderately negative under the influence of Span 80 and Tween 80/SDS. Therefore, the electrostatic attraction between oil droplets and the H0 membrane surface changed to electrostatic repulsion and contributed to decreasing membrane fouling. Thien et al. also reported that the surfactant-stabilized oil droplets and surfactant-soaked membranes have the same charges due to surfactant adsorption, independent of surfactant type [49], leading to electrostatic repulsion.

However, the fouling behavior of the H0 membrane and the H20 membrane for the positively charged Span 80 and CTAB stabilized microemulsions (62.67 ± 0.76 mV) was different compared with the two previous microemulsions (Fig. 10c). The H0 membrane showed the least membrane fouling compared with the other two types of microemulsions due to strong electrostatic repulsion between the positively charged membrane surface (14.1 ± 3.8 mV) and oil droplet. A higher reversible and irreversible fouling was found for the H20 membrane (Fig. 10d), compared to the H0 membrane, due to the electrostatic attraction. The reason probably is that, although CTAB molecular

Table 1
Properties of the Al$_2$O$_3$ and SiC-coated membranes.

Sample name	Coating time (min)	Pore size (nm)	Permeance (L m^{-2} h^{-1} bar^{-1})
H0	0	41	380
H20	20	35	195
H0-200	0	81	498
H20-200	20	62	235
H0-600	0	181	985
H20-600	20	139	827

adsorbed on the H20 membrane surface, charge inversion was not observed for the H20 membrane with a highly negatively charged surface, which was supported by the observation of a decrease of zeta potential from −55.4 mV to −30.9 mV. Therefore, the CTAB and Span 80 stabilized microemulsions fouled the H20 membrane rapidly.

3.5.3. Fouling behavior with various membrane pore sizes

Based on the findings of previous researchers, the early stage of colloidal fouling is characterized by pore blocking [54]. Specifically, in this work, oil droplets smaller than the diameter of membrane pores can result in pore blocking, whereas droplets much bigger than membrane pores can result in the cake layer formation. As shown in Fig. 11 a-c and Table 1, the oil rejection decreased with the increase of the membrane pore sizes. When the average pore sizes of the membranes were far less than the average particle size of oil droplets, the membranes were more effective at retaining the oil droplets due to the pore size sieving effect. As a result, the oil rejection rate of the H0 membrane (41 nm) and the H20 membrane (35 nm) were 99.4 % and 99.2 %, respectively (Fig. 11a and e). When the mean pore sizes further increased to 139 nm (H20-600) and 181nm (H0-600), the sieving capacity of pore size was reduced. Therefore, it was less probable that the nano-sized oil droplets would pass through the pores of membrane, leading to the lowest oil rejection rate of 71.3 % (H20-600) and 54.9 % (H0-600) (Fig. 11c and e). It is noticeable that the particle size distribution of the microemulsion revealed that 40.3 % of the oil droplets had a size below 80 nm. Interestingly, the 81 nm H0-200 membrane demonstrated an oil rejection of 94.2 % (Fig. 11b and e). The phenomenon observed can be attributed to the deposition of nano-sized oil droplets on the membrane surface during the initial stage of the filtration process, resulting in the formation of a cake layer and subsequent rejection of the nano-sized droplets. To verify the build-up of the cake layer, the oil rejection was measured at three different time intervals: 0 to 2 min, 2 to 4 min, and 4 to 20 min in every cycle of the experiment using the H0-200 membranes. The results depicted in Fig. 11b indicate that there was an observed rise in oil rejection from 85.6 % to 93.6 % for the H0-200 membrane in the first cycle, which confirmed the cake layer formation. Besides, the large percentage of reversible fouling shown in Fig. 11d verified that the dominant fouling mechanism was cake filtration. A similar phenomenon was also observed for the H20-200, H0-600, and H20-600 membranes. As expected, the irreversible fouling decreased as the pore size increased. Particularly, the irreversible fouling of the H0 membrane was significantly greater than that of the other membranes since higher TMP led oil droplets to deform and go into pores. Overall, considering the fouling resistance and a constant oil rejection over 98 % after the cake layer formed, the 62 nm H20-200 membrane is a promising choice for the separation of the microemulsions.

3.6. Long term filtration performance of the SiC-coated membrane

We assessed the long-term performance of the SiC-coated membrane (H20) by conducting O/W separation for 1000 min (20 min per cycle with backwashing between cycles), as shown in Fig. 12. Initially, during the early stage of the filtration process (within the first 160 min), the H20 membrane showed a relatively fast fouling tendency, requiring backwashing of the H20 membrane every 20 min. After the first eight
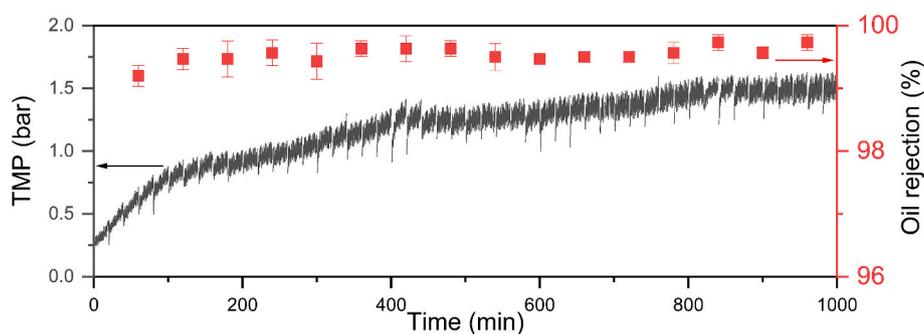
Fig. 12. Fouling behavior of the H20 membrane for 1000 min during the filtration of microemulsions stabilized with 50 mg/L Span 80 and 50 mg/L SDS at the salinity of 1 mM.

Table 2
Comparison of the optimum membrane in this work with other reported hydrophilic ceramic membranes for oil/water separation.

Membrane	Pore size (nm)	Water permeance ($Lm^{-2} h^{-1} bar^{-1}$)	Oil droplet size (nm)	Rejection (%)	Ref
αAl_2O_3-ZrO_2	50	80	1360	>90	[59]
ZrO_2	78	300.55	18	99.7	[1]
Si_3N_4	680	260	680	91	[55]
Graphene oxide	220	534	100–500	99.9	[56]
SiC	710	654	50–200	93.5	[13]
SiC	400	324	1000	98.5	[58]
ZrO_2/SiC	60	300	1350	99.9	[57]
SiC	430	300	850	90	[28]
SiC-coated Al_2O_3	47	177	5000	99	[9,15]
SiC-coated Al_2O_3	35	195	99	99.7	This work
SiC-coated Al_2O_3	62	235	99	96.2	This work
SiC-coated Al_2O_3	139	827	99	71.3	This work

cycles, the H20 membranes reached a dynamic stable filtration status with both a low per-cycle TMP increase and a high recovery of water permeance. Besides, the oil rejection during the fifty-cycle filtration experiments was 99.6 ± 0.2 %. After soaking the H20 membrane in citric acid (0.01 M, 70 °C) for 60 min, the permeance of the H20 membrane could be recovered to 99 %, showing the reusability of the SiC-coated membranes.

3.7. Comparison with other ceramic membranes

Different hydrophilic ceramic membranes for oil/water separation are described in Table 2, based on the membrane pore size, water permeance, and the rejection of oil droplets. Compared with ceramic MF membrane, the SiC-coated alumina membrane in this work has a smaller pore size and a higher oil rejection, although the water permeance is lower [13,28,55,56]. Moreover, to the best of our knowledge, the SiC membrane (H20) of this work had the smallest membrane pore size (35 nm) used for oil/water separation compared with other reported state-of-the-art SiC membranes [9,15,28,57,58].

4. Conclusion

The preparation and characterization of a pristine Al_2O_3 membrane (H0) and, innovatively, chemically stable SiC-coated Al_2O_3 UF membranes (H10, H15, H20, H25) and the fouling of these membranes by surfactant-stabilized O/W microemulsions was studied. A comparative analysis was conducted to examine the physicochemical properties (e.g., surface morphologies, mechanical strength, and wettability) of both Al_2O_3 membrane (H0) and SiC-coated Al_2O_3 UF membranes. Co-surfactant Span 80 was combined with three different surfactants, non-ionic Tween 80, anionic SDS, and cationic CTAB, to prepare the microemulsions. Fouling experiments were carried out at a constant flux of 80 $Lm^{-2} h^{-1}$, which was around the threshold flux. To study the influence of electrostatic interactions on membrane fouling, membrane filtration experiments were conducted at various pHs, surfactant types, and pore sizes. The findings are summarized as follows. Firstly, polycrystalline 3C-SiC deposition decreased the porosity and pore size of the membrane and improved its bending strength. Secondly, SiC-coated membranes with different deposition times, filtering O/W microemulsions, had a lower (ir)reversible fouling compared with the pristine Al_2O_3 membranes due to a more hydrophilic and negatively charged surface. The 20 min SiC-coated membranes showed the lowest (ir)reversible fouling and a lower (ir)reversible fouling was observed at higher pH due to the larger electrostatic repulsive force between the more negatively charged membrane surface and nano-sized oil droplets. Thirdly, the Al_2O_3 membrane filtering microemulsions stabilized with Span 80 and Tween 80/SDS showed a higher fouling tendency than the SiC-coated Al_2O_3 membrane due to stronger electrostatic repulsion. However, the SiC-coated Al_2O_3 membranes showed a higher fouling tendency for the positively charged (CTAB-stabilized) microemulsion than the Al_2O_3 membrane due to the electrostatic interactions (attraction for the SiC-coated Al_2O_3 membrane and repulsion for the Al_2O_3 membrane). Lastly, the 62 nm SiC-coated membrane performed best for the filtration of the microemulsion, because of the high rejection of the oil droplets and the low fouling tendency.

CRediT authorship contribution statement

Guangze Qin: Writing – original draft, Validation, Resources, Methodology, Investigation, Data curation, Conceptualization. **Asif Jan:** Methodology, Data curation. **Qi An:** Methodology, Data curation. **Hanxiao Zhou:** Methodology, Data curation. **Luuk C. Rietveld:** Writing – review & editing, Supervision, Project administration, Conceptualization. **Sebastiaan G.J. Heijman:** Writing – review & editing, Supervision, Project administration, Methodology, Conceptualization.

Declaration of competing interest

The authors declare that they have no known competing financial interests or personal relationships that could have appeared to influence the work reported in this paper.

Data availability

Data will be made available on request.

Acknowledgments

Appendix A. Supplementary data

Supplementary data to this article can be found online at https://doi.org/10.1016/j.desal.2024.117655.

References

[1] X. Wang, K. Sun, G. Zhang, F. Yang, S. Lin, Y. Dong, Robust zirconia ceramic membrane with exceptional performance for purifying nano-emulsion oily wastewater, Water Res. 208 (2022) 117859.

[2] G. Qin, The Effect of Surface Charge on Threshold Flux and Fouling Behavior of Silicon Carbide Membrane With O/W Emulsion and Sodium Alginate Solution as Typical Pollutants, 2021.

[3] A. Alborzi, I.M. Hsieh, D. Reible, M. Malmali, Analysis of fouling mechanism in ultrafiltration of produced water, J. Water Process Eng. (2022) 49.

[4] S.E. Weschenfelder, M.J.C. Fonseca, B.R.S. Costa, C.P. Borges, Influence of the use of surfactants in the treatment of produced water by ceramic membranes, J. Water Process. Eng. (2019) 32.

[5] M. Çakmakce, N. Kayaalp, I. Koyuncu, Desalination of produced water from oil production fields by membrane processes, Desalination 222 (1–3) (2008) 176–186.

[6] W.E. Odiete, J.C. Agunwamba, Novel design methods for conventional oil-water separators, Heliyon 5 (5) (2019) e01620.

[7] H.X. Xu, J.T. Liu, L.H. Gao, Y.T. Wang, X.W. Deng, X.B. Li, Study of oil removal kinetics using cyclone-static microbubble flotation column, Sep. Sci. Technol. 49 (8) (2014) 1170–1177.

[8] A. El-Hamouz, H.S. Hilal, N. Nassar, Z. Mardawi, Solid olive waste in environmental cleanup: oil recovery and carbon production for water purification, J. Environ. Manag. 84 (1) (2007) 83–92.

[9] M. Chen, S.G.J. Heijman, M.W.J. Luiten-Olieman, L.C. Rietveld, Oil-in-water emulsion separation: fouling of alumina membranes with and without a silicon carbide deposition in constant flux filtration mode, Water Res. 216 (2022) 118267.

[10] L. Yu, M. Han, F. He, A review of treating oily wastewater, Arab. J. Chem. 10 (2017) S1913–S1922.

[11] S.N. Wan Ikhsan, N. Yusof, F. Aziz, A.F. Ismail, J. Jaafar, W.N. Wan Salleh, N. Misdan, Superwetting materials for hydrophilic-oleophobic membrane in oily wastewater treatment, J. Environ. Manag. 290 (2021) 112565.

[12] N.A. Ahmad, P.S. Goh, Z. Abdul Karim, A.F. Ismail, Thin film composite membrane for oily waste water treatment: recent advances and challenges, Membranes (Basel) 8 (4) (2018).

[13] M. Xu, C. Xu, K.P. Rakesh, Y. Cui, J. Yin, C. Chen, S. Wang, B. Chen, L. Zhu, Hydrophilic SiC hollow fiber membranes for low fouling separation of oil-in-water emulsions with high flux, RSC Adv. 10 (8) (2020) 4832–4839.

[14] D. Lu, T. Zhang, J. Ma, Ceramic membrane fouling during ultrafiltration of oil/water emulsions: roles played by stabilization surfactants of oil droplets, Environ. Sci. Technol. 49 (7) (2015) 4235–4244.

[15] M. Chen, R. Shang, P.M. Sberna, M.W.J. Luiten-Olieman, L.C. Rietveld, S.G. J. Heijman, Highly permeable silicon carbide-alumina ultrafiltration membranes for oil-in-water filtration produced with low-pressure chemical vapor deposition, Sep. Purif. Technol. 253 (2020).

[16] A. Gupta, H.B. Eral, T.A. Hatton, P.S. Doyle, Nanoemulsions: formation, properties and applications, Soft Matter 12 (11) (2016) 2826–2841.

[17] D.J. McClements, Nanoemulsions versus microemulsions: terminology, differences, and similarities, Soft Matter 8 (6) (2012) 1719–1729.

[18] S.F. Anis, B.S. Lalia, R. Hashaikeh, N. Hilal, Hierarchical underwater oleophobic electro-ceramic/carbon nanostructure membranes for highly efficient oil-in-water separation, Sep. Purif. Technol. 275 (2021).

[19] Q. Cheng, D. Ye, C. Chang, L. Zhang, Facile fabrication of superhydrophilic membranes consisted of fibrous tunicate cellulose nanocrystals for highly efficient oil/water separation, J. Membr. Sci. 525 (2017) 1–8.

[20] S.J. Gao, Y.Z. Zhu, F. Zhang, J. Jin, Superwetting polymer-decorated SWCNT composite ultrathin films for ultrafast separation of oil-in-water nanoemulsions, J. Mater. Chem. A 3 (6) (2015) 2895–2902.

[21] E. Eray, V.M. Candelario, V. Boffa, H. Safafar, D.N. Østedgaard-Munck, N. Zahrtmann, H. Kadrispahic, M.K. Jørgensen, A roadmap for the development and applications of silicon carbide membranes for liquid filtration: recent advancements, challenges, and perspectives, Chem. Eng. J. 414 (2021).

[22] G. Foti, Silicon carbide: from amorphous to crystalline material, Appl. Surf. Sci. 184 (1–4) (2001) 20–26.

[23] H. Pham, C. Fan, G. Pandraud, F. Creemer, P. Sarro, N. Van der Pers, P. Visser, K. Kwakernaak, Very thin SiC membranes for micromachined vacuum sensors, in: SENSORS, 2008 IEEE, IEEE, 2008.

[24] A.A.R. Abdel-Aty, Y.S.A. Aziz, R.M.G. Ahmed, I.M.A. ElSherbiny, S. Panglisch, M. Ulbricht, A.S.G. Khalil, High performance isotropic polyethersulfone membranes for heavy oil-in-water emulsion separation, Sep. Purif. Technol. 253 (2020).

[25] Z. Pan, S. Cao, J. Li, Z. Du, F. Cheng, Anti-fouling TiO2 nanowires membrane for oil/water separation: synergetic effects of wettability and pore size, J. Membr. Sci. 572 (2019) 596–606.

[26] H. Nagasawa, T. Omura, T. Asai, M. Kanezashi, T. Tsuru, Filtration of surfactant-stabilized oil-in-water emulsions with porous ceramic membranes: effects of membrane pore size and surface charge on fouling behavior, J. Membr. Sci. (2020) 610.

[27] T. Sano, Y. Kawagoshi, I. Kokubo, H. Ito, K. Ishida, A. Sato, Direct and indirect effects of membrane pore size on fouling development in a submerged membrane bioreactor with a symmetric chlorinated poly (vinyl chloride) flat-sheet membrane, J. Environ. Chem. Eng. 10 (2) (2022).

[28] Q. Jiang, Y. Wang, Y. Xie, M. Zhou, Q. Gu, Z. Zhong, W. Xing, Silicon carbide microfiltration membranes for oil-water separation: pore structure-dependent wettability matters, Water Res. 216 (2022) 118270.

[29] B. Morana, G. Pandraud, J.F. Creemer, P.M. Sarro, Characterization of LPCVD amorphous silicon carbide (a-SiC) as material for electron transparent windows, Mater. Chem. Phys. 139 (2–3) (2013) 654–662.

[30] D. Hopkinson, M. Zeh, D. Luebke, The bubble point of supported ionic liquid membranes using flat sheet supports, J. Membr. Sci. 468 (2014) 155–162.

[31] L. Yan, P. Li, W. Zhou, Z. Wang, X. Fan, M. Chen, Y. Fang, H. Liu, Shrimp shell-inspired antifouling chitin nanofibrous membrane for efficient oil/water emulsion separation with in situ removal of heavy metal ions, ACS Sustain. Chem. Eng. 7 (2) (2019) 2064–2072.

[32] H. Zhan, T. Zuo, R. Tao, C. Chang, Robust tunicate cellulose nanocrystal/palygorskite nanorod membranes for multifunctional oil/water emulsion separation, ACS Sustain. Chem. Eng. 6 (8) (2018) 10833–10840.

[33] P. Le Clech, B. Jefferson, I.S. Chang, S.J. Judd, Critical flux determination by the flux-step method in a submerged membrane bioreactor, J. Membr. Sci. 227 (1–2) (2003) 81–93.

[34] S.P. Beier, G. Jonsson, Critical flux determination by flux-stepping, AICHE J. 56 (7) (2009) 1739–1747.

[35] R. Shang, A. Goulas, C.Y. Tang, X. de Frias Serra, L.C. Rietveld, S.G.J. Heijman, Atmospheric pressure atomic layer deposition for tight ceramic nanofiltration membranes: synthesis and application in water purification, J. Membr. Sci. 528 (2017) 163–170.

[36] B.C. Huang, Y.F. Guan, W. Chen, H.Q. Yu, Membrane fouling characteristics and mitigation in a coagulation-assisted microfiltration process for municipal wastewater pretreatment, Water Res. 123 (2017) 216–223.

[37] J. Xing, H. Liang, C.J. Chuah, Y. Bao, X. Luo, T. Wang, J. Wang, G. Li, S.A. Snyder, Insight into Fe(II)/UV/chlorine pretreatment for reducing ultrafiltration (UF) membrane fouling: effects of different natural organic fractions and comparison with coagulation, Water Res. 167 (2019) 115112.

[38] J. Li, S. Guo, Z. Xu, J. Li, Z. Pan, Z. Du, F. Cheng, Preparation of omniphobic PVDF membranes with silica nanoparticles for treating coking wastewater using direct contact membrane distillation: electrostatic adsorption vs. chemical bonding, J. Membr. Sci. 574 (2019) 349–357.

[39] Y. Lin, C.H. Loh, L. Shi, Y. Fan, R. Wang, Preparation of high-performance Al 2 O 3 /PES composite hollow fiber UF membranes via facile in-situ vapor induced hydrolyzation, J. Membr. Sci. 539 (2017) 65–75.

[40] Q. Gu, T.C.A. Ng, Y. Bao, H.Y. Ng, S.C. Tan, J. Wang, Developing better ceramic membranes for water and wastewater Treatment: Where microstructure integrates with chemistry and functionalities, Chem. Eng. J. (2022) 428.

[41] S. Huang, R.H.A. Ras, X. Tian, Antifouling membranes for oily wastewater treatment: interplay between wetting and membrane fouling, Curr. Opin. Colloid Interface Sci. 36 (2018) 90–109.

[42] J. Drelich, E. Chibowski, Superhydrophilic and superwetting surfaces: definition and mechanisms of control, Langmuir 26 (24) (2010) 18621–18623.

[43] Y. Teng, Y. Wang, B. Shi, X. Li, Y. Chen, Robust superhydrophobic surface fabrication by fluorine-free method on filter paper for oil/water separation, Polym. Test. 91 (2020).

[44] M. Yang, P. Hadi, X. Yin, J. Yu, X. Huang, H. Ma, H. Walker, B.S. Hsiao, Antifouling nanocellulose membranes: how subtle adjustment of surface charge lead to self-cleaning property, J. Membr. Sci. 618 (2021).

[45] S. Salmón-Vega, R. Herrera-Urbina, C. Lira-Galeana, M.A. Valdez, The effect of ionic surfactants on the electrokinetic behavior of asphaltene from a Maya Mexican oil, Pet. Sci. Technol. 30 (10) (2012) 986–992.

[46] J. Zhang, X. Huang, Y. Xiong, W. Zheng, W. Liu, M. He, L. Li, J. Liu, L. Lu, K. Peng, Spider silk bioinspired superhydrophilic nanofibrous membrane for efficient oil/water separation of nanoemulsions, Sep. Purif. Technol. 280 (2022).

[47] S. Kasemset, Z. He, D.J. Miller, B.D. Freeman, M.M. Sharma, Effect of polydopamine deposition conditions on polysulfone ultrafiltration membrane properties and threshold flux during oil/water emulsion filtration, Polymer 97 (2016) 247–257.

[48] Y.-M. Lin, G.C. Rutledge, Separation of oil-in-water emulsions stabilized by different types of surfactants using electrospun fiber membranes, J. Membr. Sci. 563 (2018) 247–258.

[49] T.A. Trinh, Q. Han, Y. Ma, J.W. Chew, Microfiltration of oil emulsions stabilized by different surfactants, J. Membr. Sci. 579 (2019) 199–209.

[50] M. Matos, G. Gutiérrez, A. Lobo, J. Coca, C. Pazos, J.M. Benito, Surfactant effect on the ultrafiltration of oil-in-water emulsions using ceramic membranes, J. Membr. Sci. 520 (2016) 749–759.

[51] Q. Zhang, Y. Fan, N. Xu, Effect of the surface properties on filtration performance of Al2O3–TiO2 composite membrane, Sep. Purif. Technol. 66 (2) (2009) 306–312.

[52] Y. He, K. Xu, X. Feng, L. Chen, Z. Jiang, A nonionic polymer-brush-grafted PVDF membrane to analyse fouling during the filtration of oil/water emulsions, J. Membr. Sci. 637 (2021).

[54] W. Tomczak, M. Gryta, Application of ultrafiltration ceramic membrane for separation of oily wastewater generated by maritime transportation, Sep. Purif. Technol. 261 (2021).

[55] H. Abadikhah, C.-N. Zou, Y.-Z. Hao, J.-W. Wang, L. Lin, S.A. Khan, X. Xu, C.-S. Chen, S. Agathopoulos, Application of asymmetric Si3N4 hollow fiber membrane for cross-flow microfiltration of oily waste water, J. Eur. Ceram. Soc. 38 (13) (2018) 4384–4394.

[56] X. Zhao, Y. Su, Y. Liu, Y. Li, Z. Jiang, Free-standing graphene oxide-palygorskite nanohybrid membrane for oil/water separation, ACS Appl. Mater. Interfaces 8 (12) (2016) 8247–8256.

[57] F.E. Bortot Coelho, N.N. Kaiser, G. Magnacca, V.M. Candelario, Corrosion resistant ZrO2/SiC ultrafiltration membranes for wastewater treatment and operation in harsh environments, J. Eur. Ceram. Soc. 41 (15) (2021) 7792–7806.

[58] Q. Jiang, J. Zhou, Y. Miao, S. Yang, M. Zhou, Z. Zhong, W. Xing, Lower-temperature preparation of SiC ceramic membrane using zeolite residue as sintering aid for oil-in-water separation, J. Membr. Sci. 610 (2020).

[59] J. Milić, I. Petrinić, A. Goršek, M. Simonič, Ultrafiltration of oil-in-water emulsion by using ceramic membrane: Taguchi experimental design approach, Open Chem. 12 (2) (2014) 242–249.